

# Automatic Early-Onset Free Flap Failure Detection for Implantable Biomedical Devices

Michael A. Rothfuss Nicholas G. Franconi Alexander Star Murat Akcakaya Michael L. Gimbel Ervin Sejdić

**Abstract—Objective:** Up to 10% of free flap cases are compromised, and without prompt intervention, amputation and even death can occur. Hourly monitoring improves salvage rates, but the gold standard for monitoring requires experienced personnel to operate and suffers from high false-positive rates as high as 31% that result in costly and unnecessary surgeries. In this paper, we investigate free flap patency monitoring using automatic hardware-only classification systems that eliminate the need for experienced personnel. The expected flow ranges of the antegrade and retrograde veins for breast reconstruction are studied using a syringe pump to create the laminar flow seen in veins. **Methods:** Feature data extracted from the Doppler blood flow signals are analyzed for sensitivity, specificity, and false-positive rates. Hardware is built to perform the classification automatically in real-time and output a decision at the end of the observation period. **Results:** Experimental results using the hardware-only classifier for a 50 ms window size show high sensitivity (96.75%), specificity (90.20%), and low false-positive rate (9.803%). The experimental and theoretical classification results show close agreement. **Conclusion:** This work indicates that automatic hardware-only classifiers can eliminate the need for experienced personnel to monitor free flap patency. **Significance:** The hardware-only classification is amenable to a monolithic implementation and future studies should study a totally implantable wirelessly-powered blood flow classifier. The high classifier performance in a short window period indicates that duty-cycled powering can be used to extend the safe operational depth of an implant. This is particularly relevant for the difficult buried free flap applications.

**Keywords:** Biomedical monitoring, blood flow, feature classification, free flap, patency

## I. INTRODUCTION

Hourly blood vessel patency monitoring in the first few days after free flap surgery is crucial to the survival of the free flap transferred tissue [1]. Loss of flow, if not caught promptly, can result in loss of the free flap [2], amputation [3], and death [4]. Up to 10% of free flap cases are compromised in post-operative monitoring period [5]. Furthermore, the gold standard for free flap monitoring, the Cook-Swartz Doppler Probe and System, has a false positive rate up to 31% for some flap types (i.e., head and neck [6]), leading to expensive re-exploration (i.e., \$20k-\$30k per case) [7].

Michael A. Rothfuss, Nicholas G. Franconi, Murat Akcakaya, and Ervin Sejdić are with the Department of Electrical and Computer Engineering, Swanson School of Engineering, University of Pittsburgh, Pittsburgh, PA, 15261 USA. E-mails: mar28@pitt.edu, ngf3@pitt.edu, akcakaya@pitt.edu, esejdic@ieee.org

Alexander Star is with the Department of Chemistry, University of Pittsburgh, Pittsburgh, PA, 15260 USA. E-mail: astar@pitt.edu.

Michael L. Gimbel is with the Department of Plastic Surgery, University of Pittsburgh, Pittsburgh, PA, 15261 USA. E-mail: gimbelml@upmc.edu.

The gold standard uses a transcutaneous wire that tethers a patient to a bedside monitor. The tether is intentionally designed to be lightly tugged to dislodge from the implanted probe at the end of the monitoring period. Unfortunately, this wire can be snagged resulting damage to the vessel or dislodging, causing loss of signal. It is this wire that is responsible for the device's high false positive rate [8], [9]. Typically, the flap's venous outflow is a better indicator of flap patency, compared to monitoring arterial flow. However, the venous flow signature is often difficult to distinguish from background noise. As a result, experienced personnel are needed to interpret the gold standard's output [10], [11]. Our prior work in wireless implantable patency monitors for the peripheral veins provided a simple visual output for clinicians to determine patency [12]. From a clinical and usability perspective, our prior work had three shortcomings: the baseline flow must be recorded to determine future flow status, and an experienced clinician is still need to interpret the simple output. Another shortcoming of the device was its high power budget required to digitize blood flow waveform signals and transmit the data wirelessly to an external receiver for further processing.

In this paper, we investigate automatic decision making circuits for blood flow applications. Feature extraction and decision-making circuitry developed by Gestner et al. [13] for glass break detection are investigated for their use in automatic real-time patency detection. There are several advantages to approaching patency monitoring this way. First, experienced personnel are completely eliminated from the decision making process (i.e., to improve false positive rates). Second, a patency threshold can be incorporated into the design. Swartz et al. reports that poor blood flow signals (i.e., very low flow rates) are indicators of likely flap compromise [14]). Thus, we investigate using blood flow rate thresholds to establish a critical intervention point for early free flap failure detection. And lastly, the low current consumption of the feature extraction and automatic decision making circuits (i.e., Gestner et al. report 20  $\mu\text{A}$  in a 0.35  $\mu\text{m}$  process for their glass break detector) make them amenable to a microchip implementation for integration into a wireless implantable medical device [15]. In a microchip implementation, all of the blood flow information processing is performed in real-time and on the implant, meaning that only a simple "yes" or "no" status would need to be transmitted at the end of a measurement period. Thus, the precious radio frequency spectrum usage is significantly reduced compared to devices that transmit the digitized Doppler blood flow signal, such as in our previous work [12].

In this paper, we investigate automatic decision making circuits for blood flow applications. Feature extraction and decision-making circuitry developed by Gestner et al. [13] for glass break detection are investigated for their use in automatic real-time patency detection. There are several advantages to approaching patency monitoring this way. First, experienced personnel are completely eliminated from the decision making process (i.e., to improve false positive rates). Second, a patency threshold can be incorporated into the design. Swartz et al. reports that poor blood flow signals (i.e., very low flow rates) are indicators of likely flap compromise [14]. Thus, we investigate using blood flow rate thresholds to establish a critical intervention point for early free flap failure detection. And lastly, the low current consumption of the feature extraction and automatic decision making circuits (i.e., Gestner et al. report 20  $\mu\text{A}$  in a 0.35  $\mu\text{m}$  process for their glass break detector) make them amenable to a microchip implementation for integration into a wireless implantable medical device [15]. In a microchip implementation, all of the blood flow information processing is performed in real-time and on the implant, meaning that only a simple “yes” or “no” status would need to be transmitted at the end of a measurement period. Thus, the precious radio frequency spectrum usage is significantly reduced compared to devices that transmit the digitized Doppler blood flow signal, such as in our previous work [12].

The high false-positive rates of the gold standard and the need for early-onset free flap failure detection without clinical interpretation motivate the experiments herein. We incorporate portions of our previously developed wireless implanted blood flow monitors along with the feature extraction and classification hardware, to determine the effect of measurement window size on measurement sensitivity, specificity, and false positive rates. As a proof of concept, we study patency detection for the venous flow ranges in the antegrade and retrograde mammary veins [16].

There are three main contributions of this paper. First, this is the first automatic blood flow patency classifier. This patency classifier is intended to be used in place of experienced personnel for determining when to surgically intervene in the case of patency failure in free flap surgeries. Second, we select features that are appropriate for blood flow and are amenable to a hardware implementation, and we show how observation window size affects the sensitivity, specificity, and false-positive rates for detecting patency failures. And lastly, this is the first application of Gestner et al.’s work to biomedical monitoring (i.e., Gestner et al.’s work focused only on glass break detection) as well as the first circuit implementation (i.e., Gestner et al.’s work was only simulated and not experimentally verified) of analog feature extraction and classification for the difficult-to-interpret blood flow in veins. We demonstrate the implemented electronics for flow rates expected in a breast reconstruction scenario.

## II. METHODOLOGIES

### A. The Doppler Signal and Its Features

The insonifying acoustic wave that impinges on red blood cells (RBCs) scatters isotropically with an intensity pro-

portional to  $f^4$  (i.e., Rayleigh scattering), so long as the wavelength of the wave is much larger than the RBCs and RBC aggregates [17]. The energy is scattered at a frequency proportional to the velocity of the RBCs [18]. The baseband Doppler signal is extracted from the scattered signal using a zero-IF mixer, where the resulting signal’s frequency content represents the velocity of the RBCs. The Doppler frequency,  $f_d$ , is proportional to the velocity of the RBCs and is defined by the well-known Doppler equation:

$$f_d = \frac{2f_0 v \cos(\theta)}{c} \quad (1)$$

where  $f_0$  is the insonifying frequency,  $\theta$  is the angle between the piezoelectric transducer face and the blood vessel wall,  $v$  is the RBC velocity in the sample volume, and  $c$  is the speed of sound in blood (i.e., approximately  $1586.7 \pm 3 \text{ m/s}$  average across available literature for human blood [17]).

Blood flow profile has a significant influence on the Doppler signal [19]. Arterial flow is typically described by turbulent flow (i.e., more pulsatile), while venous flow is typically described by laminar flow. Because venous outflow is a better predictor of flap patency, we focus our research on venous flows [14]. Swartz et al. indicates that when a blood flow waveform begins to diminish, suggesting a very low flow rate, free flap compromise is likely. The lack of available literature for the threshold cut-off flow rate that prompts surgical intervention motivates the reason for demonstrating our experiments for a useful example application – the antegrade and retrograde mammary veins in free flap breast reconstruction. Venturi et al. conveniently report the flow rates for these veins for all of their patients [16]. The range of antegrade vein flow rates are 1.96 mL/min and 9.76 mL/min ( $4.88 \pm 3.17 \text{ mL/min}$ ) and the range of retrograde vein flow rates are 1.62 mL/min and 10.61 mL/min ( $3.47 \pm 2.71 \text{ mL/min}$ ). In the two veins, for patency classification purposes, flow rate data below approximately 50% of the lowest flow rate are labeled as no-flow, while those data above this threshold are labeled as flow. This labeling method was similarly used by Heller et al. to indicate a warning threshold to prompt monitoring a flap more closely [20].

Many features can be extracted from Doppler signals for automatic diagnostic systems [21]; however, these algorithms are suited for execution on computer hardware, meaning that very few features are amenable to a mixed-signal hardware implementation, much less a monolithic implementation for biomedical implants. Gestner et al.’s work in glass break detectors showed 100% automatic classification accuracy for a database of glass-break, noise, music, and speech sounds [13]. Gestner’s device extracted total signal energy, high-band signal energy, and zero-crossing features. Conveniently, the Doppler signal lies within the range of audible human hearing [22].

Therefore, we choose to investigate automatic blood flow classification using zero-crossing and signal energy features using Gestner et al.’s techniques. Zero-crossing rate (ZCR) (i.e., the number of high-to-low and low-to-high signal transitions across the zero point on the y-axis in a desired period) detection has a long history of use in the Doppler ultrasound

field for estimating blood flow [23], [24], [25]. ZCR is an important feature because it provides an estimate of the mean Doppler frequency [18]. Signal energy is also a natural feature candidate because absolute no-flow clearly presents only a noise signal, while flow clearly presents signal components proportional to RBC velocity. In this research, we investigate a classifier using the signal energy and zero-crossing definitions shown in Eqs. (2) and (3) for each window segment,  $x$ :

Signal energy:

$$E_x = \mathbf{max}(x[n]) \quad (2)$$

Zero-crossing:

$$\text{ZCR}_x = \sum_1^{n-1} \text{floor} \left( \mathbf{H} \left[ \frac{\text{sign}(x[n-1]) - \text{sign}(x[n])}{2} \right] \right) \quad (3)$$

where  $\mathbf{H}$  is the Heaviside function. Note that these equations are intended to approximate the transfer function of the energy and ZCR detector circuits of Section II-B. The energy function approximates a peak detector, and the ZCR function increments whenever the Doppler signal sign changes from positive to negative (i.e., a negative-going signal).

### B. System Hardware Design

Figure 1 shows the implemented printed circuit board (PCB) and its associated schematic and constituent components. The Analog Front-End is used to insonify the blood sample volume, using the transmit (TX) piezoelectric transducer, and then amplify the received signal, from the receive (RX) piezoelectric transducer, and then extract the baseband Doppler blood flow signal. The Analog Front-End and piezoelectric transducers are based off of our previous work in wireless implantable blood flow monitors [12]. The zero-crossing rate feature extractor and energy feature extractor are based off of Gestner et al.'s work [13] in monolithic glass break detectors. The ZCR circuit charges a charge storage capacitor with a short pulse each time a negative-going (i.e., signal amplitude crossing the zero axis from positive to negative) signal is detected. Preliminary data showed the ZCR circuit range needed to generate its output proportional to up to about 8 kHz. The energy feature extractor circuit is an envelope detector (i.e., peak detector). The feature data are extracted by sampling the ZCR and energy signals,  $V_{\text{ZCR}}$  and  $V_{\text{ENERGY}}$ , respectively after a pre-defined period, called the window size. The sampled ZCR and energy signals are  $V_{\text{ZCR,SH}}$  and  $V_{\text{ENERGY,SH}}$ , respectively. The Clock & Timing Management handles clock synthesis, signal sampling (i.e., window size), and synchronizing system events. The Feature Classification implements a variation of Gestner et al.'s monolithic decision circuitry suitable for blood flow patency detection. That is to say, compared to Gestner et al.'s work, the feature classification implementation in this work implements a 2-dimensional discriminative hyperplane, using discrete electronics, that classifies the ZCR and total signal energy features extracted from blood flow signals. Whereas, Gestner et al.'s 3-dimensional discriminative hyperplane classified ZCR, total signal energy, and high-band energy extracted from glass break sounds using

only simulated monolithic circuits. The extracted sampled ZCR and energy feature voltages are classified as being on one side of the dividing hyperplane or the other.  $V_{\text{PATENCY}}$  is high when flow is detected and low when no-flow is detected.

### C. Early-Onset Free Flap Failure Classification

For the purpose of determining sensitivity and specificity, we define true positives, false positives, true negatives, and false negatives of free flap patency the same as used by Kempton et al. for their breast reconstruction free flap monitoring study [26]. That is to say, true positives are defined as a loss of signal for a compromised flap, false positives are defined as a loss of signal for a viable flap, true negatives are defined as a flow signal present for a viable flap, and false negatives are defined as flow signal present for a compromised flap. Additionally, sensitivity may be referred to as the true positive rate (TPR), and specificity may be referred to as the true negative rate (TNR).

The effect of window size on the features obtained from the Doppler signal are not known. Therefore, we investigate the effects that window size has on sensitivity, specificity, and false positive rates by applying Eqs. (2) and 3 on the Doppler signals at each window size. Clearly, using a smaller window size is preferred, as longer window sizes incur long measurement times, larger device power consumption (i.e., especially for battery powered devices), and move further away from real-time monitoring, etc.

Early-onset free flap failure detection is accomplished by labeling flow rates below 50% of the lowest flow rate described in Section II-A (i.e.,  $1/2 \times 1.62 \text{ mL/min} = 0.81 \text{ mL/min}$ ). We use the nearest  $1/4 \text{ mL}$  as the threshold:  $0.75 \text{ mL/min}$ . Therefore, flow rates below this threshold are labeled as “no flow” and flow rates above, and including, this threshold are labeled as “flow.” Flow measurements near this threshold are expected to be often classified incorrectly when the data are not clearly separable, so window sizes that improve feature data separability are expected to have better sensitivity, specificity, and false positive rates.

### D. Experimental Setup and Data Collection Procedure

Figure 2 shows the experimental data collection setup. The equipment shown includes: two Vector Signal Generators (VSG), a 50 mL HSW Norm-Ject syringe (inner diameter: 29.2 mm) driving a long length of heat-shrink tubing (inner diameter: 4.75 mm) mounted in an NE-1000 syringe pump (New Era Pump Systems, Inc., Farmingdale, NY), a blood phantom with simulated red blood cells (P/N: BRS185-Doppler, Blue Phantom, Sarasota, FL), a Saleae Logic 8 logic analyzer (Saleae, Inc., San Francisco, CA), a battery powered laptop computer (i.e., to prevent equipment ground loops), a 250 mL beaker, a custom-built long wooden channel to maintain the entrance length to achieve laminar flow (i.e., at least 4.75 cm) [27], two 20 MHz piezoelectric transducers in a Continuous Wave Doppler (CWD) configuration inset to a 5 mm inner diameter silicon cuff (Iowa Doppler Products, Iowa City, IA), and the circuit hardware described in Section II-B. The laptop computer used here is solely for the purpose of operating the

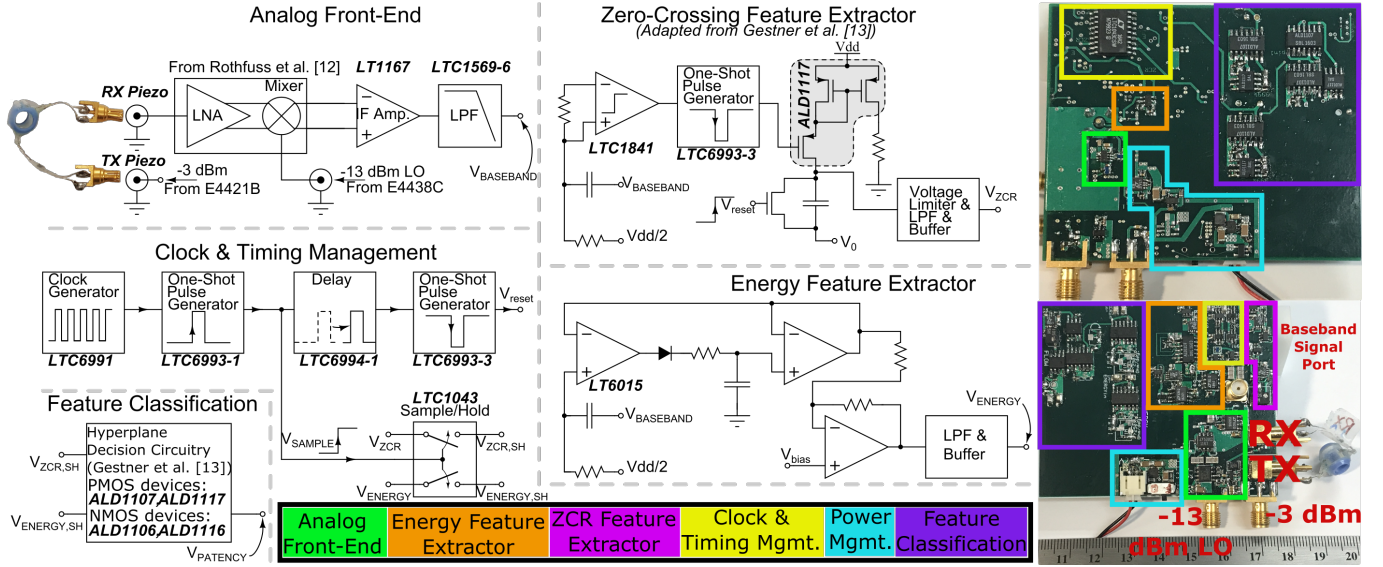


Fig. 1. Doppler signal processing and feature extraction/classification schematic and the corresponding PCB.

Saleae Logic 8 logic analyzer and storing the data collected by the logic analyzer for offline processing. Under normal operating conditions, the feature classification circuitry has been already configured to generate an appropriate 2-dimensional discriminative hyperplane based on the processed offline data, and thus the Saleae Logic 8 logic analyzer and laptop computer are not used to determine patency.

The E4421B VSG driving the TX piezoelectric transducer is set to -3 dBm at 20 MHz, and the E4438C VSG driving the mixer's local oscillator (LO) port is set to -13 dBm at 20 MHz (i.e., to provide approximately 300 mV<sub>pp</sub> LO drive). The -3 dBm TX piezoelectric transducer drive power results in sufficiently large baseband signal levels without introducing distortion; larger TX piezoelectric transducer drive powers result in supply railings in the baseband amplifier and signal processing stages of the Analog Front-End. E4421B VSG is synchronized to the E4438C reference frequency signal.

The syringe pump, syringe and heat-shrink tubing, wooden channel, piezoelectric transducers, and blood phantom were the same used in our prior study on wireless implantable blood flow monitors [12]. The syringe is over-filled with 60 mL of the blood phantom to collect all data in succession without needing to adjust the setup for refilling. Air gaps between the silicon cuff/transducers and the heat-shrink tubing were filled with generic ultrasound gel. The beaker collects expelled blood phantom fluid. A data collection begins by programming the syringe pump at the desired flow rate. Once the pumping has started, referring to Figure 1, the baseband Doppler signal, feature extraction outputs,  $V_{ZCR,SH}$  and  $V_{ENERGY,SH}$ , sample clock output  $V_{SAMPLE}$ , and feature classification output,  $V_{PATENCY}$ , are collected using the Saleae Logic 8 logic analyzer and stored on the laptop computer for offline processing. Data is collected for 30 seconds at flow rates 0 mL/min, 0.5 mL/min, 0.75 mL/min, and 1 mL/min to 10 mL/min in 1 mL/min increments (i.e., totaling 13 flow rates) using a 50 ms window size.

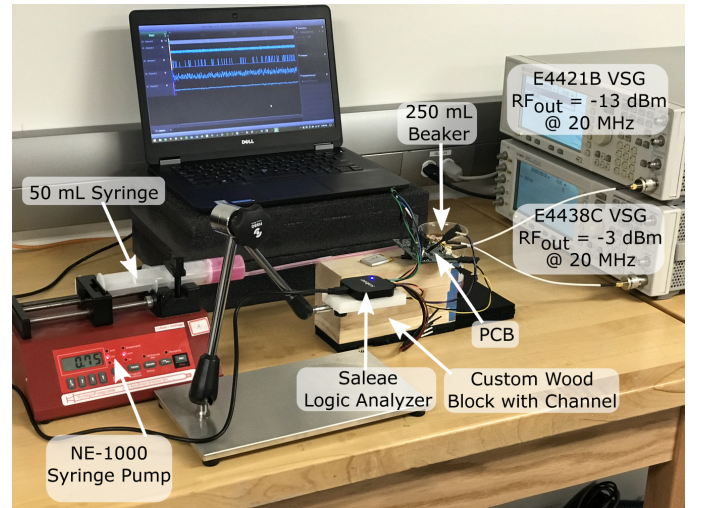


Fig. 2. Setup for the experimental data measurements.

Two of the 13 flow rate data collections are required to generate and test the hyperplane created by circuits described in Section II-B. We use the same Ho-Kashyap procedure used by Gestner et al. [13] for generating a classification hyperplane line offline. From the first data collection, a 10 K-fold cross-validation procedure is used to generate 10 hyperplane classification lines offline. Then, the feature classification circuitry is modified to generate a hyperplane to match the average of these 10 lines. The second data collection tests the classification capabilities of the circuit hyperplane, generated from the first data collection. The measured patency decision estimate,  $V_{PATENCY}$ , is compared to the labeled flow rate data to compute the sensitivity, specificity, and false positive rate of the designed circuitry.

Programmed flow rate accuracy is confirmed using Eq. (4),  $Q_{avg}$  is the average volumetric flow rate of the blood in the vessel,  $f_0$  is the ultrasonic insonifying frequency, 20 MHz,

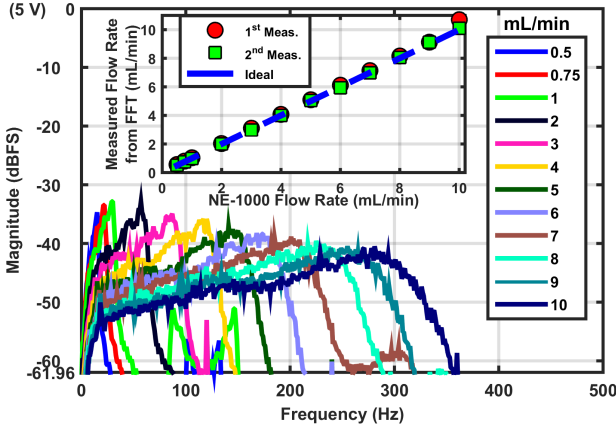


Fig. 3. Spectrum from each programmed flow rate. Each 30 second Doppler signal is split into 50 segments and their FFT's averaged. The Saleae Logic 8's analog-to-digital (ADC) converter uses a 10-bit 5V full scale (4.883 mV LSB).

$\theta = 45^\circ$ ,  $A = 0.18 \text{ cm}^2$  inside circular cross-sectional area of heat shrinking tubing, and  $f_{\max}$  is the maximum Doppler frequency,  $f_{\max}$ , is estimated as about half-way below the peak spectral amplitude along the steep downward sloping section of the spectrum, as demonstrated by Vilkomerson et al. for laminar flows [28]. We obtain the Doppler spectrum from a measured Doppler signal by, first, splitting the 30 second signal into 50 equal-length segments, second, using the fast Fourier transform (FFT) [29] on each segment to transform the segments into their spectral equivalent, and then finally, averaging the spectral magnitude of the same spectral bin across all 50 segments.

$$Q_{avg} = A \cdot \frac{c}{2f_0 \cos(\theta)} \frac{f_{\max}}{2} \frac{60 \text{ sec.}}{\text{min.}} \quad (4)$$

### III. RESULTS

#### A. Hardware Performance Evaluation

Figure 3 shows the measured flow rates from the first and second data collections compared to the ideal expected flow rate. In the figure, a flow rate is determined by extracting  $f_{\max}$  from the flow rate's spectrum and then applying Eq. (4). The accuracy across all measured flow rates for the first data collection was  $0.1434 \pm 0.1815 \text{ mL/min}$  and for the second data collection  $0.0387 \pm 0.0418 \text{ mL/min}$ . This result confirms the accuracy of the syringe pump setup and affirms the baseband Doppler signal input to feature extraction circuitry.

Figures 4(a)-(b) benchmark the feature extraction circuitry for a 50 ms window size. These circuits process the Doppler signal at their inputs (i.e., from  $V_{\text{BASEBAND}}$  from Figure 1). The energy feature extractor output is shown as a function of mean input amplitude to show the circuit's peak detection performance. The energy feature extractor performs well for signals above approximately 20 mV for frequencies above 20 Hz. The ZCR feature extractor results uncover an important aspect of this system's design: accurate ZCR detection requires a large input signal drive (i.e., at  $V_{\text{BASEBAND}}$ ), especially

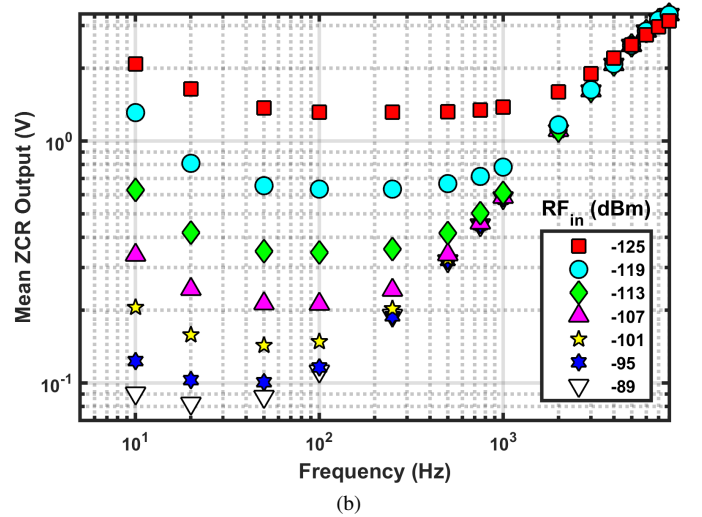
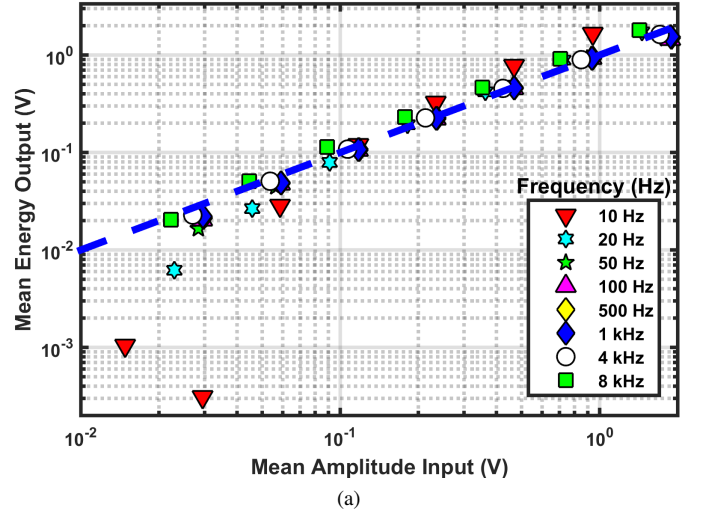


Fig. 4. Feature extraction circuitry benchmarking for a 50 ms window size: (a) Energy. Dotted line shows ideal transfer function. (b) Zero-Crossing Rate (ZCR)

for frequencies below a few hundred Hertz. Figure 5 shows both the frequency response (i.e., from the *RX Piezo* port to  $V_{\text{BASEBAND}}$ ) and the mean baseband amplitude at  $V_{\text{BASEBAND}}$  as a function of the LNA input power. The 0 dB gain frequency occurs at 500 Hz, and the low-frequency and high-frequency half-voltage levels occur at 10 Hz and approximately 11 kHz, respectively. Using Eq. (4) and setting  $f_{\max}$  equal to these half-voltage frequencies, the corresponding flow rates are 0.2982 mL/min for 10 Hz and 328.0 mL/min for 11 kHz, which covers the bandwidth of all possible flow rates in our experiments (i.e., see Figure 3). Examining the ZCR feature extraction results from Figure 4(b) along with Figure 5, the required LNA input power can be determined to maximize ZCR accuracy. A larger LNA input power requires a proportionally larger TX piezoelectric device drive power, which unfortunately increases the burden for the electronics driving the TX piezoelectric device.

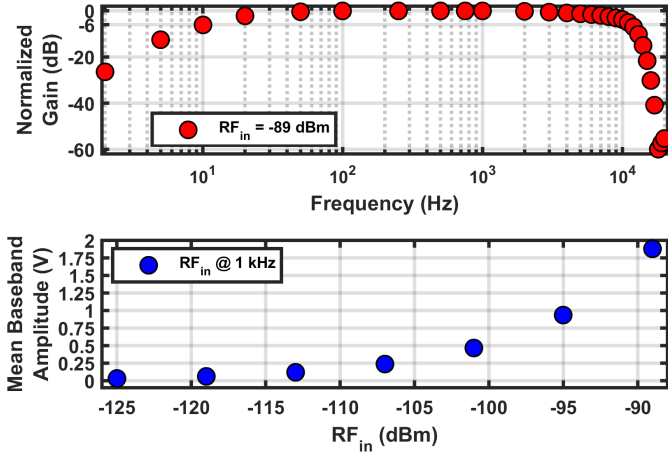


Fig. 5. Frequency response of the Analog Front-End and the mean baseband amplitude for a given input power at the LNA input.

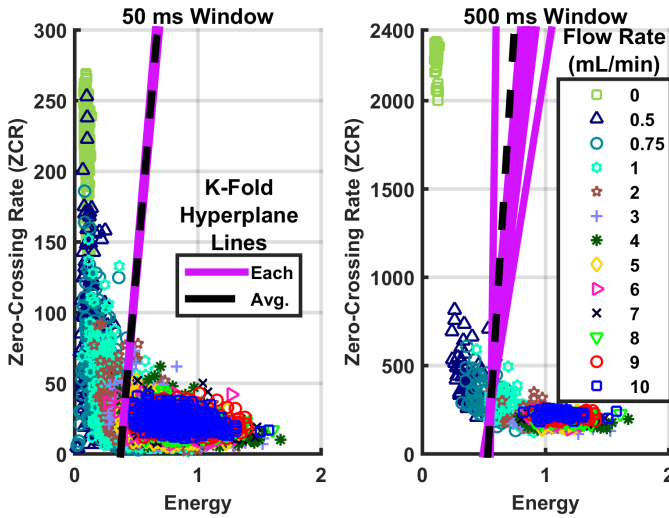


Fig. 6. Feature classification using Eqs. (2) and (3) showing each K-fold hyperplane and the average K-fold hyperplane line for a 50 ms and 500 ms window size.

### B. Feature Extraction, Equation-Based Classification, and Windowing

Figure 6 shows feature classification performed using Eqs. (2) and (3) at 50 ms and 500 ms window sizes. This figure shows the effect window size has on the resulting feature values. As expected, a larger window size results in larger ZCR values. Also, the feature value spread is smaller as window size increases, improving separability for classification, thereby reducing misclassification and improving the sensitivity, specificity, and the false-positive rate.

Figure 7(a) shows the sensitivity and specificity and Figure 7(b) shows the false-positive rates resulting from classification performed using Eqs. (2) and (3) from window sizes ranging from 0.5 ms to 1 sec. Note that little improvement in sensitivity, and sometimes a degradation, is seen after approximately a 50 ms window size. At small window sizes the capture period is too short for the ZCR feature to be meaningful: all of the flow and no-flow signals exhibit nearly the same ZCR for small window sizes. As the window size increases, more of the

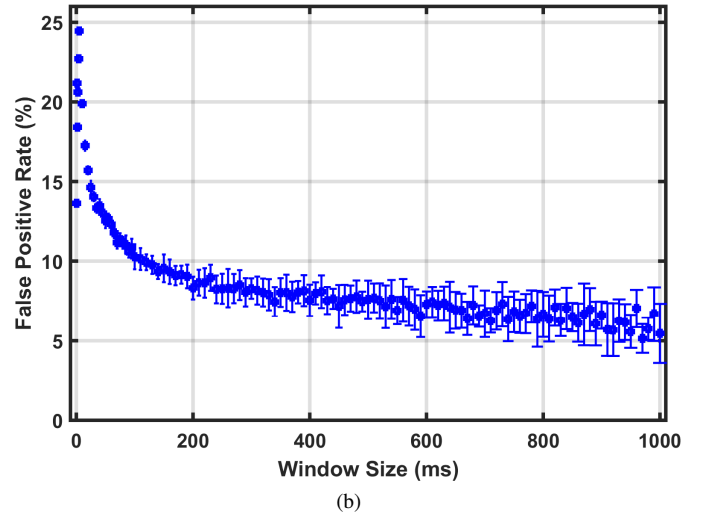
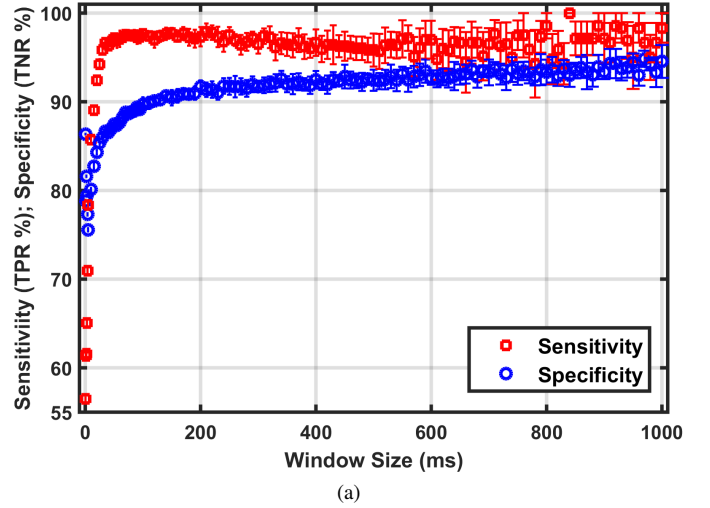


Fig. 7. Using Eqs. (2) and (3); Error bars are the standard error ( $\frac{\sigma}{\sqrt{n}}$ ): (a) Mean sensitivity and mean specificity. (b) Mean false-positive rate.

Doppler signal bandwidth and noise bandwidth (i.e., the lower energy high ZCR data) can be captured, which shifts the flow rate feature data towards clusters. The clusters are more readily separable when calculating the discriminating hyperplane lines that determining the sensitivity, specificity, and false-positive rates. Meanwhile, the specificity and false-positive rate improve marginally but consistently as window size increases. At a 50 ms window size, and using  $\mu \pm SE$  where SE is the standard error defined as  $\frac{\sigma}{\sqrt{n}}$ , the mean sensitivity is  $97.17 \pm 0.3557\%$ , the mean specificity is  $87.47 \pm 0.4618\%$ , and the mean false-positive rate is  $12.53 \pm 0.4618\%$ . Comparatively, at a 500 ms window size, the mean sensitivity is  $95.83 \pm 1.863\%$ , the mean specificity is  $92.42 \pm 1.195\%$ , and the mean false-positive rate is  $7.576 \pm 1.195\%$ .

### C. Automatic Hardware Classification

Figure 8(a)–(c) shows the experimentally measured energy and ZCR feature voltage values along with classification hyperplanes. Figure 8(a) shows the measured feature values from the first data collection. The experimentally measured hyperplane circuit transfer function is matched closely to the

TABLE I

FINAL CLASSIFICATION RESULTS FOR MEAN SENSITIVITY, SPECIFICITY, AND FALSE-POSITIVE RATES ON MEASURED DATA COMPUTED FROM EQS. (2) – (3), THE AVERAGE HYPERPLANE FROM 10 K-FOLD CROSS-VALIDATION (I.E., THE DASHED LINE IN FIGURE 8(B)), AND THE HARDWARE-BASED CLASSIFIER (I.E., FROM THE MEASURED HYPERPLANE IN FIGURE 8(B); MEASURED  $V_{\text{PATENCY}}$ ) PERFORMANCE. DATA EXPRESSED AS  $\mu \pm \text{SE}$ , WHERE STANDARD ERROR (SE) IS DEFINED AS  $\frac{\sigma}{\sqrt{n}}$ .

	Sensitivity (%)	Specificity (%)	False-Positive Rate (%)
Eqs. (2) – (3)	97.17±0.3557	87.47±0.4618	12.53±0.4618
Avg. of K-Folds	97.33±0.4444	90.32±0.3973	9.682±0.3973
$V_{\text{PATENCY}}$	96.75	90.20	9.803

resulting hyperplane from the average of the 10 K-fold cross-validation of the first data collection. Figure 8(b) shows the second data collection features values with the experimentally measured hyperplane circuit transfer function and the resulting hyperplane from the average of the 10 K-fold cross-validation on this second data collection. Note the slight change in K-fold cross-validation hyperplane compared to the experimentally measured hyperplane circuit transfer function. The slight change does not affect the results much because the experimentally measured hyperplane circuit transfer function nearest the feature values is still approximately the same as the K-fold cross-validation hyperplane. Table I summarizes the classification performance for the second data collection for equation-based classification of the Doppler signal (i.e., using Eqs. (2) – (3)), for the K-fold cross-validation classification of the experimentally measured feature values, and for the experimentally measured  $V_{\text{PATENCY}}$  decision output from the classification circuit. The close agreement between the equation-based classification (i.e., using Eqs. (2) – (3)) and the hardware-only classification (i.e., using  $V_{\text{PATENCY}}$ ) indicates that implementations of the classification hardware can be accurately predicted mathematically.

Figure 8(c) employs a majority vote to the measured feature values at each flow rate. A majority vote accumulates decision output data over some observation period and the majority wins the overall decision. The majority vote method of patency detection is better for deciding on whether to perform a surgical re-exploration or not, especially in the case of low flow rates, which border the discriminative hyperplane but still within the normal range of the vein. In a 30 second data collection, there are 600 observations for a 50 ms window size; thus each stacked column sums to 600. The majority vote uncovers an important result: even if the patency decision at the end of the measurement window period is a misclassification (i.e., contributing to the false-positive rate), aggregating decisions will produce a more accurate result, and a decrease surgical re-exploration.

#### IV. DISCUSSION

Smit et al. described the elements of the ideal microvascular free flap monitor by five core tenets: can be easily deployed, its output easily understandable by inexperienced personnel,

deployable and operable at any site, doesn't cause patient discomfort, and provides reliable and continuous monitoring [30]. The last point being the most important for this study. To the best of the authors' knowledge, there has been no reported literature investigating free flap failure and patency detection through automatic classification methods. Our prior work on wireless implantable blood flow monitors for patency detection required personnel to interpret signal voltage magnitudes [12]. Our current research demonstrated automatic classification of blood flow that completely eliminated the need for human interpretation. Additionally, this work improved upon our prior work by automatically detecting diminished flow before the absolute no-flow was reached.

Existing methods for Doppler signal classification are based on software algorithms that require significant computational resources (i.e., desktop/laptop computers), as described in Übeyli and Güler's review on Doppler signal features for automated diagnoses [21]. Blood flow monitoring for free flap patency detection needs to eliminate the transcutaneous wire tether found in the gold standard Cook-Swartz blood flow monitor [8], [9], which requires a wireless implantable blood flow monitor, such as in our prior work [12]. However, using existing Doppler signal classification methods with these wireless blood flow monitors would require externally processing the blood flow data. Externally processing the blood flow data requires significant power resources on the implant, in order to digitize and wirelessly transmit the blood flow data with sufficient fidelity in real-time (i.e., one of Smit et al.'s tenets – reliable and continuous monitoring). In addition to wirelessly transmitting the sampled signal (i.e., and whatever bandwidth it occupies), a common telemetry technique to reduce power consumption from the high-frequency radio electronics requires the maximizing radio idle time (i.e., radio powered-down) and to transmit data in high data-rate bursts [31]. The high data-rate bursts occupy significant amount of the allocated radio frequency spectrum and a high carrier frequency, which results in shorter link ranges [32] and significant signal attenuation due to lossy dielectric tissues [33]. As discussed by Mandal and Sarpeshkar, high-data rate biomedical implant telemetry carries regulatory concerns, and few unlicensed bands below 433 MHz have channel bandwidths greater than a few hundred kilohertz. Therefore, our research presents a technological leap forward in patency detection: as low as one symbol/sec needs to be transmitted for real-time patency monitoring. That is to say, one or multiple windowed classification decisions can be acquired each second, then a majority vote can be transmitted, requiring a single symbol to indicate a “yes” or “no” of patency status. A review and comparison of existing published implantable wireless blood flow monitors is reported by Rothfuss et al. [34]. Notable devices include: Yonezawa et al.'s device frequency modulated an 82 MHz carrier frequency directly with the 25 kHz Doppler signal [24], Vilkomerson's device operating in the 402–405 MICS band transmitting at 200 kpb/s [35], and Rothfuss' device operated at 433 MHz transmitting at 500 kBaud [12]; all transmit the entire blood flow signal and require large implantable batteries, which would cause patient discomfort, violating one of Smit et al.'s tenets.

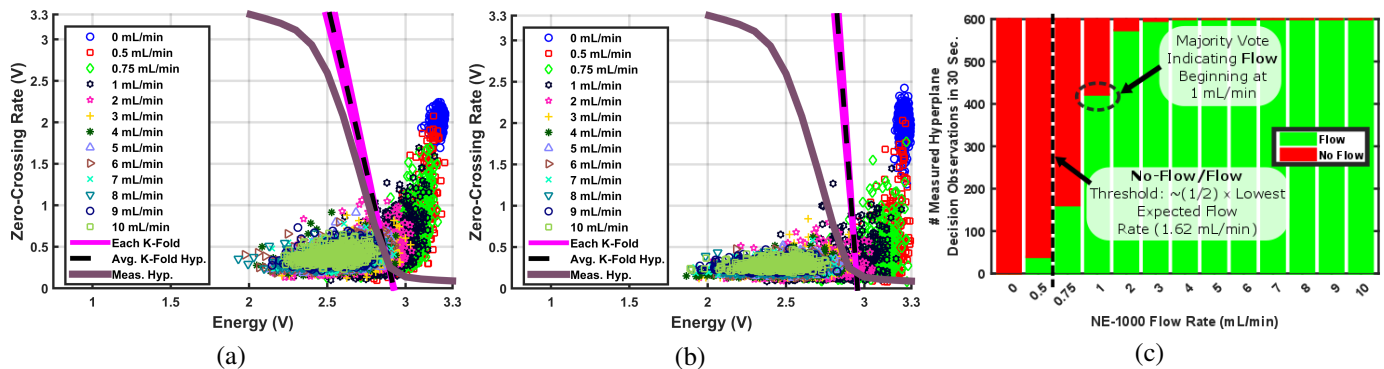


Fig. 8. (a) Initial data collection used to find an average K-fold hyperplane to match the measured hyperplane circuit transfer properties. (b) Final data collection showing measured hyperplane circuit transfer properties from the initial data collection along with the calculated K-fold hyperplanes of the final data collection. (c) Accumulated measured observations of patency status at each flow rate.

We expanded on the work reported by Gestner et al. [13], which was originally intended only for glass-break detection, and had not envisioned alternative applications of their technology. Through our research, we demonstrated the efficacy of the hardware-only blood flow classifier for patency detection, and additionally, we found, and demonstrated, that this classifier can be used for the early detection of future free flap failures. The advantage of the hardware-only classifier is that it is amenable to a monolithic microchip for implantation, which carries significant reductions in size and power, compared to previously developed wireless implantable blood flow monitors, such as by DiPietro and Meindl (i.e.,  $< 36 \text{ cm}^3$  at 10 mW) [23], Vilkomerson et al. (i.e., two PCBs; PCB<sub>1</sub>:  $\sim 3.5 \times 5.5 \text{ cm}$ ; PCB<sub>2</sub>:  $\sim 2.5 \times 4.9 \text{ cm}$  at  $\sim 105 \text{ mW}$ ) [35], and Rothfuss et al. (i.e.,  $< 1.7 \text{ cm}^3$  at 444 mW) [34], which are all battery powered and can only be powered-on for a few seconds per day to achieve a long implant lifetime. Note the differences in power consumption and that DiPietro and Meindl used some custom monolithic chips for blood flow monitoring, while Vilkomerson et al. and Rothfuss et al. used discrete commercial off-the-shelf parts. The power consumption for an eventual monolithic implementation of this classifier for blood flow applications is expected to approximate Gestner et al.'s reported power consumption, 20  $\mu\text{A}$  for a Taiwan Semiconductor Manufacturing Company (TSMC) 0.35  $\mu\text{m}$  process, or about about 66  $\mu\text{W}$  – 100  $\mu\text{W}$ , which is well within the safety limits for wirelessly powered bioimplants (i.e., hundreds of  $\mu\text{W}$ 's – to mW's [36], [37]), leaving a relatively large power budget for other on-chip electronics.

Our results for window size trends indicate that beyond approximately a 50 ms window size, only small improvements are gained in false positive rate, meaning that a biomedical implant could report a patency estimate in the time required to power-on an implant plus the window size time. Our prior work in implanted stents as energy harvesters for powering biomedical implants [38] showed that a wirelessly powered battery-less implant could reach power-on in 200  $\mu\text{s}$ , meaning the window size dominates the time required to obtain a patency estimate. Often, in order to meet safety limits for wireless power transmission through tissue, the power-on time of an implant will be duty cycled. Wireless power link gains from the external power transmitter to the implant are typically

very poor, especially for deep-seated implants (i.e.,  $> 2 \text{ cm}$ ). This means that for a deep implant, the wireless power will need to be increased in order to deliver sufficient power to the implant, but the increase in transmitted power will require a lower duty cycle to meet safety limits. Our results for window size provide valuable insight into the expected false positive rate penalty or improvement that could be expected when powering a deep implanted patency monitor, such as for buried flaps [8], [6], requiring a low duty cycle powering scheme. This result also suggests that as a wirelessly powered implant for buried flaps, this work would be a good candidate to also satisfy another one of Smit et al.'s tenets – operational at any site.

Monitoring depths below 2 cm are difficult to impossible for the Cook-Swartz's nearest free flap competing technologies – Laser Doppler flowmetry and Near-Infrared Spectroscopy (NIRS) [30]. The lowest reported power consumption for an implantable wireless blood flow monitor was 10 mW, reported by DiPietro and Meindl [23]. From our prior work with implanted stent energy harvesters, a 5% duty cycle (i.e., a 50 ms window size, as used in our experimental measurements in this study) would make approximately 26.75 mW safely available to the implanted electronics at an implant depth of 3.36 cm (i.e., 0.19 cm skin, 1.1 cm fat, and 2.07 cm muscle) for a small external antenna for power delivery and communication [38]. Conversely, for the same implant depth and the same external antenna size, a 20% duty cycle (i.e., a 200 ms window size) would make approximately 6.69 mW safely available. From Figure 7, the mean false-positive rates for the 50 ms and 200 ms window sizes would be  $12.53 \pm 0.4618\%$  and  $8.303 \pm 0.7174\%$ , respectively. It should be noted that, in our wireless implantable stent study operating in the 100 – 400 MHz band, the 2 W/kg limit averaged over 10 grams of tissue imposed by the two commonly referenced standards, the IEEE Standard C95.1-2005 [39] and the International Commission on Non-Ionizing Radiation Protection (ICNIRP) [40], impose a 30 minute and 6 minute exposure period, respectively. One of Smit et al.'s tenets describes the ideal blood flow monitor as providing continuous/real-time feedback [30]. This implies that the false-positive rate cannot simply be improved by arbitrarily using large window sizes. Very large window sizes clearly require a long implant powered-on time, which would

occupy a large portion of the regulatory exposure periods, and subsequently prevent the continuous/real-time feedback tenet by Smit et al.

The gold standard's false positive rates can be very high, as much as 31% [6], and often vary widely throughout literature. The primary cause for the high false positives is the device's transcutaneous wire tether [9]. Consider the classifier investigated in this research as part of a biomedical implant, thus implying that the wire tether is eliminated as a source of false positives. Our results show that flow rates near the classification line (see Figure 8(c)) are responsible for the feature value misclassifications that result in false-positives. Using the majority vote method to make a decision on whether to operate would reduce the effective false-positive rate more than those found in Figure 7(b) – the majority vote results suggest that the flap would still be patent at 1 mL/min, which is below the 1.62 mL/min lowest expected flow rate but above the ~50% programmed threshold. Thus, the classifier in this study, along with majority voting, would completely prevent an unnecessary and costly surgical re-exploration for the flow ranges studied in this paper, corresponding to the expected flow ranges in the antegrade and retrograde veins in breast reconstruction.

## V. CONCLUSION

This paper showed a hardware-only free flap patency monitoring system, capable of detecting flap failures before they happen, that provided a simple binary output indicator of free flap patency status and did not require any operator experience to interpret. We validated the hardware-only classification automatic classification method for patency detection in flow ranges expected in the antegrade and retrograde veins during breast reconstruction. Our results showed that hardware free flap patency classifiers showed high sensitivity, specificity, and low false positive rates compared to the gold standard for free flap monitoring. Accumulating patency estimate observations uncovered the hardware classification's capability to detect failure before absolute no-flow was reached. The results of this study indicated that this patency classifier should be implemented as part of a wirelessly-powered monolithic biomedical implant to investigate its ability to detect free flap failures automatically, without the need for experienced personnel and while eliminating the troublesome transcutaneous wire tether found in the gold-standard.

## REFERENCES

- [1] F. Hölzle, A. Rau, D. Loeffelbein, T. Mücke, M. Kesting, and K.-D. Wolff, "Results of monitoring fasciocutaneous, myocutaneous, osteocutaneous and perforator flaps: 4-year experience with 166 cases," *International Journal of Oral and Maxillofacial Surgery*, vol. 39, no. 1, pp. 21–28, 2010.
- [2] S. S. Kroll, M. A. Schusterman, G. P. Reece, M. J. Miller, G. R. Evans, G. L. Robb, and B. J. Baldwin, "Timing of pedicle thrombosis and flap loss after free-tissue transfer," *Plastic and Reconstructive Surgery*, vol. 98, no. 7, pp. 1230–1233, 1996.
- [3] F.-C. Wei, F. Demirkan, H.-C. Chen, D. Chuang, S. Chen, C.-H. Lin, S.-L. Cheng, M.-H. Cheng, and Y.-T. Lin, "The outcome of failed free flaps in head and neck and extremity reconstruction: what is next in the reconstructive ladder?" *Plastic and Reconstructive Surgery*, vol. 108, no. 5, pp. 1154–60, 2001.

- [4] C. E. Attinger, I. Ducic, C. L. Hess, A. Basil, M. Abbruzzesse, and P. Cooper, "Outcome of skin graft versus flap surgery in the salvage of the exposed Achilles tendon in diabetics versus nondiabetics," *Plastic and Reconstructive Surgery*, vol. 117, no. 7, pp. 2460–2467, 2006.
- [5] K. Z. Paydar, S. L. Hansen, D. S. Chang, W. Y. Hoffman, and P. Leon, "Implantable venous doppler monitoring in head and neck free flap reconstruction increases the salvage rate," *Plastic and Reconstructive Surgery*, vol. 125, no. 4, pp. 1129–1134, 2010.
- [6] R. E. H. Ferguson Jr and P. Yu, "Techniques of monitoring buried fasciocutaneous free flaps," *Plastic and Reconstructive Surgery*, vol. 123, no. 2, pp. 525–532, 2009.
- [7] J. P. Fischer, B. Sieber, J. A. Nelson, E. Cleveland, S. J. Kovach, L. C. Wu, S. Kanchwala, and J. M. Serletti, "Comprehensive outcome and cost analysis of free tissue transfer for breast reconstruction: an experience with 1303 flaps," *Plastic and Reconstructive Surgery*, vol. 131, no. 2, pp. 195–203, 2013.
- [8] J. J. Rosenberg, B. D. Fornage, and P. M. Chevray, "Monitoring buried free flaps: limitations of the implantable Doppler and use of color duplex sonography as a confirmatory test," *Plastic and Reconstructive Surgery*, vol. 118, no. 1, pp. 109–113, 2006.
- [9] T. Zhang, D. Dyalram-Silverberg, T. Bui, J. F. Caccamese, and J. E. Lubek, "Analysis of an implantable venous anastomotic flow coupler: experience in head and neck free flap reconstruction," *International Journal of Oral and Maxillofacial Surgery*, vol. 41, no. 6, pp. 751–755, 2012.
- [10] J. M. Porter, G. L. Moneta, and An International Consensus Committee on Chronic Venous Disease, "Reporting standards in venous disease: an update," *Journal of Vascular Surgery*, vol. 21, no. 4, pp. 635–645, 1995.
- [11] A. I. Galeandro, G. Quistelli, P. Scicchitano, M. Gesualdo, A. Zito, P. Caputo, R. Carbonara, G. Galgano, F. Ciciarello, S. Mandolesi, C. Franceschi, and M. M. Ciccone, "Doppler ultrasound venous mapping of the lower limbs," *Vascular Health and Risk Management*, vol. 8, p. 59, 2012.
- [12] M. A. Rothfuss, N. G. Franconi, J. V. Unadkat, M. L. Gimbel, A. Star, M. H. Mickle, and E. Sejdic, "A system for simple real-time anastomotic failure detection and wireless blood flow monitoring in the lower limbs," *IEEE Journal of Translational Engineering in Health and Medicine*, vol. 4, pp. 1–15, 2016.
- [13] B. Gestner, J. Tanner, and D. Anderson, "Glass break detector analog front-end using novel classifier circuit," in *2007 IEEE International Symposium on Circuits and Systems*. IEEE, 2007, pp. 3586–3589.
- [14] W. M. Swartz, R. Izquierdo, and M. J. Miller, "Implantable venous doppler microvascular monitoring: Laboratory investigation and clinical results," *Plastic and Reconstructive Surgery*, vol. 93, no. 1, pp. 152–163, 1994.
- [15] K. N. Bocan and E. Sejdic, "Adaptive transcutaneous power transfer to implantable devices: A state of the art review," *Sensors*, vol. 16, no. 3, p. 393, 2016.
- [16] M. L. Venturi, M. M. Poh, P. M. Chevray, and M. M. Hanasono, "Comparison of flow rates in the antegrade and retrograde internal mammary vein for free flap breast reconstruction," *Microsurgery*, vol. 31, no. 8, pp. 596–602, 2011.
- [17] P. R. Hoskins, "Physical properties of tissues relevant to arterial ultrasound imaging and blood velocity measurement," *Ultrasound in Medicine & Biology*, vol. 33, no. 10, pp. 1527–1539, 2007.
- [18] K. K. Shung, *Diagnostic Ultrasound: Imaging and Blood Flow Measurements*. CRC press, 2005.
- [19] K. K. Shung, G. Cloutie, and C. C. Lim, "The effects of hematocrit, shear rate, and turbulence on ultrasonic Doppler spectrum from blood," *IEEE Transactions on Biomedical Engineering*, vol. 39, no. 5, pp. 462–469, 1992.
- [20] L. Heller, L. S. Levin, and B. Klitzman, "Laser Doppler flowmeter monitoring of free tissue transfers: Blood flow in normal and complicated cases," *Plastic and Reconstructive Surgery*, vol. 107, no. 7, pp. 1739–1745, 2001.
- [21] E. D. Übeyli and İ. Güler, "Feature extraction from Doppler ultrasound signals for automated diagnostic systems," *Computers in Biology and Medicine*, vol. 35, no. 9, pp. 735–764, 2005.
- [22] T. L. Szabo, *Diagnostic Ultrasound Imaging: Inside Out*. Academic Press, 2004.
- [23] D. M. Di Pietro and J. D. Meindl, "Optimal system design for an implantable CW Doppler ultrasonic flowmeter," *IEEE Transactions on Biomedical Engineering*, no. 3, pp. 255–264, 1978.
- [24] Y. Yonezawa, T. Nakayama, I. Ninomiya, and W. Caldwell, "Radio telemetry directional ultrasonic blood flowmeter for use with unrestrained animals," *Medical and Biological Engineering and Computing*, vol. 30, no. 6, pp. 659–665, 1992.

- [25] J. A. Jensen, *Estimation of Blood Velocities Using Ultrasound: A Signal Processing Approach*. Cambridge University Press, 1996.
- [26] S. J. Kempton, S. O. Poore, J. T. Chen, and A. M. Afifi, "Free flap monitoring using an implantable anastomotic venous flow coupler: Analysis of 119 consecutive abdominal-based free flaps for breast reconstruction," *Microsurgery*, vol. 35, no. 5, pp. 337–344, 2015.
- [27] M. A. Fogel, *Ventricular Function and Blood Flow in Congenital Heart Disease*. John Wiley & Sons, 2008.
- [28] D. Vilkomerson, S. Ricci, and P. Tortoli, "Finding the peak velocity in a flow from its Doppler spectrum," *IEEE transactions on Ultrasonics, Ferroelectrics, and Frequency Control*, vol. 60, no. 10, pp. 2079–2088, 2013.
- [29] W. T. Cochran, J. W. Cooley, D. L. Favin, H. D. Helms, R. A. Kaenel, W. W. Lang, G. C. Maling, D. E. Nelson, C. M. Rader, and P. D. Welch, "What is the fast Fourier transform?" *Proceedings of the IEEE*, vol. 55, no. 10, pp. 1664–1674, 1967.
- [30] J. M. Smit, C. J. Zeebregts, R. Acosta, and P. M. Werker, "Advancements in free flap monitoring in the last decade: a critical review," *Plastic and Reconstructive Surgery*, vol. 125, no. 1, pp. 177–185, 2010.
- [31] A. Chandrakasan, R. Min, M. Bhardwaj, S. Cho, and A. Wang, "Power aware wireless microsensor systems," in *Proceedings of the 28th European 2002 Solid-State Circuits Conference*. IEEE, 2002, pp. 47–54.
- [32] B. Razavi, *RF Microelectronics*, ser. Prentice Hall Communications Engineering and Emerging Technologies. Castleton, New York: Prentice Hall, 2012.
- [33] S. Gabriel, R. Lau, and C. Gabriel, "The dielectric properties of biological tissues: II. measurements in the frequency range 10 Hz to 20 GHz," *Physics in Medicine and Biology*, vol. 41, no. 11, p. 2251, 1996.
- [34] M. A. Rothfuss, J. V. Unadkat, M. L. Gimbel, M. H. Mickle, and E. Sejdjić, "Totally implantable wireless ultrasonic Doppler blood flowmeters: Toward accurate miniaturized chronic monitors," *Ultrasound in Medicine & Biology*, vol. 43, no. 3, pp. 561–578, 2017.
- [35] D. Vilkomerson, T. Chilipka, J. Bogan, J. Blebea, R. Choudry, J. Wang, M. Salvatore, V. Rotella, and K. Soundararajan, "Implantable ultrasound devices," in *Medical Imaging*. International Society for Optics and Photonics, 2008, pp. 69 200C–69 200C.
- [36] A. S. Poon, S. O'Driscoll, and T. H. Meng, "Optimal frequency for wireless power transmission into dispersive tissue," *IEEE Transactions on Antennas and Propagation*, vol. 58, no. 5, pp. 1739–1750, 2010.
- [37] J. M. Rabaey, M. Mark, D. Chen, C. Sutardja, C. Tang, S. Gowda, M. Wagner, and D. Werthimer, "Powering and communicating with mm-size implants," in *2011 Design, Automation & Test in Europe Conference & Exhibition (DATE)*. IEEE, 2011, pp. 1–6.
- [38] M. A. Rothfuss, N. G. Franconi, K. N. Bocan, J. V. Unadkat, M. L. Gimbel, M. H. Mickle, and E. Sejdjić, "Can we wirelessly and safely monitor peripheral artery disease?" *IEEE Transactions on Biomedical Engineering*, 2017, Submitted.
- [39] "IEEE standard for safety levels with respect to human exposure to radio frequency electromagnetic fields, 3 kHz to 300 GHz," *IEEE Std C95.1-2005 (Revision of IEEE Std C95.1-1991)*, pp. 1–238, April 2006.
- [40] International Commission on Non-Ionizing Radiation Protection, "Guidelines for limiting exposure to time-varying electric, magnetic, and electromagnetic fields (up to 300 GHz)," *Health Physics Society*, vol. 74, no. 4, pp. 494–522, 1998.